

# Global long-term mapping of surface temperature shows intensified intra-city urban heat island extremes

Lorenzo Mentaschi (✉ [lorenzo.mentaschi@ec.europa.eu](mailto:lorenzo.mentaschi@ec.europa.eu))

European Commission, Joint Research Center, Ispra <https://orcid.org/0000-0002-2967-9593>

Gregory Duveiller

European Commission Joint Research Centre <https://orcid.org/0000-0002-6471-8404>

Grazia Zulian

European Commission, Joint Research Center, Ispra

Christina Corbane

European Commission, Joint Research Center, Ispra

Martino Pesaresi

European Commission, Joint Research Center, Ispra <https://orcid.org/0000-0003-0620-439X>

Joachim Maes

European Commission, Joint Research Center, Ispra

Alessandro Stocchino

The Hong Kong Polytechnic University

Luc Feyen

European Commission, Joint Research Centre (JRC) <https://orcid.org/0000-0003-4225-2962>

---

## Article

**Keywords:** Heat-related Human Illnesses, Short Term Heat Stress, Urbanisation, Heatwaves, Greening

**Posted Date:** March 10th, 2021

**DOI:** <https://doi.org/10.21203/rs.3.rs-251967/v1>

**License:**   This work is licensed under a Creative Commons Attribution 4.0 International License.

[Read Full License](#)

---

**Version of Record:** A version of this preprint was published at Global Environmental Change on January 1st, 2022. See the published version at <https://doi.org/10.1016/j.gloenvcha.2021.102441>.

# 1 Global long-term mapping of surface 2 temperature shows intensified intra-city 3 urban heat island extremes

4 Lorenzo Mentaschi<sup>1</sup>, Grégory Duveiller<sup>1</sup>, Grazia Zulian<sup>1</sup>, Christina Corbane<sup>1</sup>, Martino  
5 Pesaresi<sup>1</sup>, Joachim Maes<sup>1</sup>, Alessandro Stocchino<sup>2</sup>, Luc Feyen<sup>1</sup>

6 <sup>1</sup>: Joint Research Centre (JRC), European Commission, Ispra, Italy.

7 <sup>2</sup>: Department of Civil and Environmental Engineering, The Hong Kong Polytechnic University, Hong Kong.

8 **Surface temperatures are generally higher in cities than in rural surroundings<sup>1</sup>. This phenomenon, known**  
9 **as surface urban heat island (SUHI), increases the risk of heat-related human illnesses and mortality<sup>2</sup>.**  
10 **Past global studies analysed this phenomenon aggregated at city scale or over seasonal and annual time**  
11 **periods<sup>3-6</sup>, while human impacts strongly depend on shorter term heat stress experienced locally. Here**  
12 **we develop a global long-term high-resolution dataset of daytime SUHI as urban-rural surface**  
13 **temperature differences. Our results show that across urban areas worldwide over the period 2003-2020,**  
14 **3-day SUHI extremes are on average more than twice as high as the warm-season median SUHI, with**  
15 **local exceedances up to 10 K. Over this period, SUHI extremes have increased more rapidly than warm-**  
16 **season medians, and averaged worldwide are now 1.04 K or 31% higher compared to 2003. This can be**  
17 **linked with increasing urbanisation<sup>7</sup>, more frequent heatwaves<sup>8</sup>, and greening of the earth<sup>9</sup>, processes**  
18 **that are all expected to continue in the coming decades<sup>10-12</sup>. Within many cities there are hotspots where**  
19 **extreme SUHI intensity is 10 to 15 K higher compared to relatively cooler city parts. Given the limited**  
20 **human adaptability to heat stress<sup>13</sup>, our results advocate for mitigation strategies targeted at reducing**  
21 **SUHI extremes in the most vulnerable and exposed city neighbourhoods.**

22 Nowadays, more than half of the human population lives in cities and in the foreseeable future most  
23 population growth will be in urban areas<sup>10</sup>. A prominent feature of cities' climate is the Urban Heat Island  
24 (UHI), whereby the temperature of urbanized areas noticeably differs from that of rural neighbouring  
25 zones<sup>14</sup>, and is generally higher, especially in humid climates when the surroundings are covered by dense  
26 vegetation<sup>15,16</sup>. The intensity of UHI as estimated from Land Surface Temperature (LST) is usually referred to  
27 as Surface Urban Heat Island (SUHI)<sup>3</sup>.

28 Studies have found UHI intensity to be linked with background hydro-climatic conditions<sup>5,17</sup>, city size<sup>4,18</sup> and  
29 morphology<sup>19</sup>, thermodynamic properties of artificial surfaces and construction materials<sup>3-5,20</sup>, and the  
30 density and characteristics of vegetation<sup>17,21</sup>. Because most urban climate studies are performed on limited  
31 and not always representative empirical cases, it is difficult to intercompare their results and to reach  
32 general quantitative conclusions on causal relationships<sup>22</sup>.

33 A more comprehensive database of global urban surface warming is needed for identifying emerging  
34 spatiotemporal patterns and areas for remediation. Large-scale UHI studies have focused primarily on  
35 coarse-grained representations of UHIs, where the thermal behaviour is lumped spatially over urban  
36 centres<sup>23,24</sup> and temporally over seasonal<sup>5</sup> or annual<sup>3</sup> time scales. As a consequence, these fail to capture  
37 UHI peaks that are localised in space and time, and that are better represented in fine-scale studies<sup>25-27</sup>.  
38 Characterising temporal fluctuations is of foremost importance to assess the real threat posed to human  
39 health by urban heat, as phenomena such as heat waves can often last only few days<sup>28-30</sup>. Moreover, UHI  
40 intensity can vary between different parts of the same city<sup>22</sup> depending on their morphology and on the

41 thermodynamic properties of their constitutive elements (e.g. densely built-up areas vs green areas).  
42 Finally, spatial averaging can dilute the intensity of the hazard felt locally.

43 Here we estimate daytime SUHI as the difference in LST between urban pixels and their rural surroundings  
44 at 1x1 km globally with a daily time step for the period 2003-2020. We use LST retrieved from satellite  
45 observations of the MODIS Aqua mission and built-up surfaces of the Global Human Settlements Layer  
46 (GHSL)<sup>31</sup> to delineate urban pixels. We focus our analysis on the warm season, when urban heat is more  
47 likely to represent a risk to human health<sup>3,4,21</sup>. As the highest effects typically appear within 3 days of  
48 extreme heat event onset<sup>30</sup> we consider 3-day averaged values of SUHI. For each urban pixel we calculate:  
49 (1) the warm-season median ( $SUHI_{seas}$ ), which represents a central estimate of the SUHI in the warm  
50 season for each year between 2003-2020; (2) the 1-year maximum ( $SUHI_{1y}$ ), which represents the  
51 maximum 3-day SUHI in the warm season for each year between 2003-2020; and (3) the 18-year maximum  
52 ( $SUHI_{18y}$ ), which represents the maximum 3-day SUHI estimated over all the warm seasons between 2003-  
53 2020.

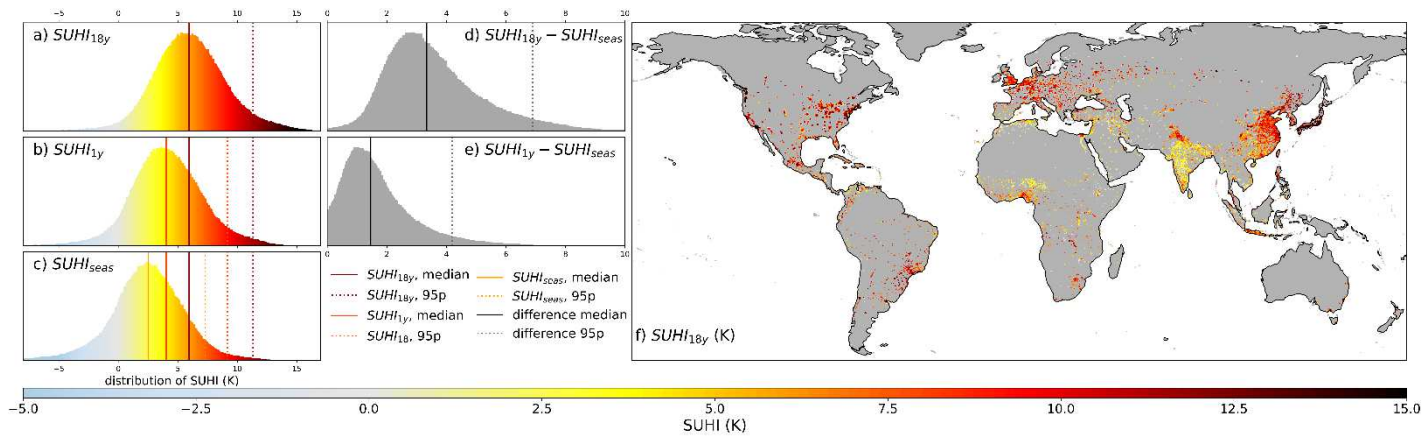
### 54 Short-term maxima versus temporally aggregated SUHI

55 Across all urban areas worldwide over the period 2003-2020, the space-time median  $SUHI_{seas}$  is 2.5 K (**Fig.**  
56 **1** and **Table S1**). This corroborates earlier global<sup>3,4</sup> and regional<sup>15</sup> studies that report annually and  
57 seasonally averaged SUHI intensities of few degrees. Short-term maxima show to be significantly higher.  
58 With a global 18-year space-time median  $SUHI_{1y}$  of 4.0 K, annual 3-day peaks of SUHI are on average 1.5 K  
59 more intense than the seasonal SUHI. Under extreme conditions of urban surface warming, represented by  
60  $SUHI_{18y}$ , this rises to nearly 6.0 K, or more than a doubling of the seasonal SUHI intensities.

61 There is large variation around the central global estimates. Extreme SUHI intensity ( $SUHI_{18y}$ ) can reach  
62 beyond 16 K, with a global 95<sup>th</sup> percentile of 11.3 K. This is about 4 K higher than the corresponding  
63 statistics for the warm-season median SUHI ( $SUHI_{seas}$ ). At pixel level,  $SUHI_{1y}$  exceeds  $SUHI_{seas}$  by a  
64 maximum of >7 K, and by 4.2 K in 5% of urban pixels. For  $SUHI_{18y}$ , the pixel-wise differences with  
65  $SUHI_{seas}$  are even larger and reach 6.9 K in 5% of urban pixels, with a maximum difference >12 K. While  
66 synergies between heat waves and SUHI have not been fully understood and remain subject of debate<sup>32</sup>,  
67 several studies have shown amplified urban warming under heat waves, especially in temperate regions<sup>33</sup>.  
68 Hence, during times when background heat is most pronounced, strongly intensified SUHI can considerably  
69 add to the heat stress in cities.

70 Eighteen percent of urban pixels present negative values of  $SUHI_{seas}$ , whilst this fraction is much reduced  
71 if maxima are considered:  $SUHI_{1y}$  is negative in 7% of the pixels and  $SUHI_{18y}$  is negative in 2.3% of the  
72 pixels. This suggests that cities, or parts thereof, that generally act as heat sinks (i.e., urban areas cooler  
73 than their surroundings<sup>4</sup>) may occasionally behave as heat islands (**Fig. S1**).

74



75

76 **Fig. 1 | Global distribution of warm-season SUHI indices.** **a**, Histogram across urban pixels worldwide of the pixel warm-season 3-  
 77 day SUHI maximum over the 18 years analysed ( $SUHI_{18y}$ ). **b**, Histogram across all urban pixels worldwide of the pixel median of the  
 78 yearly warm-season 3-day SUHI maxima ( $SUHI_{1y}$ ) of the 18 years analysed. **c**, Histogram across all urban pixels worldwide of the  
 79 pixel warm-season SUHI median ( $SUHI_{seas}$ ) over the 18 years analysed. **d**, Histogram across all urban pixels worldwide of the pixel  
 80 difference between  $SUHI_{18y}$  and the 18-year median  $SUHI_{seas}$ . **e**, Histogram across all urban pixels worldwide of the pixel  
 81 difference between  $SUHI_{1y}$  and the 18-year median  $SUHI_{seas}$ . The solid and dashed vertical lines in the histograms in a-e  
 82 represent the median and 95<sup>th</sup> percentile over all urban pixels worldwide for the respective indices and differences therein. **f**,  
 83 Global map of warm-season 3-day SUHI maximum over the 18 years analysed ( $SUHI_{18y}$ ) in urban pixels. Urban pixels are defined  
 84 as 1x1 km built-up pixels enclosed within the spatial boundaries of Functional Urban Areas (FUA). FUA are cities and their  
 85 surroundings and nearly four billion people live in the 9028 FUAs worldwide.

86

87 The global map of  $SUHI_{18y}$  (**Fig. 1f**) shows strong spatial heterogeneity in extreme surface urban warming,  
 88 but some geographic patterns can be observed linked with background climate.  $SUHI_{18y}$  is generally  
 89 higher at mid-high latitudes in areas characterized by temperate and humid conditions, where dense and  
 90 aerodynamically rough vegetation in rural areas results in higher evapotranspiration rates and convection  
 91 efficiency compared to their urban counterparts. In drier regions, evapotranspiration and convection  
 92 efficiency of low stature natural vegetation outside cities is lower, resulting in smaller or even negative UHI  
 93 intensities<sup>5,16</sup>. Monsoon and equatorial regions also show mostly milder  $SUHI_{18y}$  intensities, which relates  
 94 to a levelling of the precipitation effect on evapotranspiration above 1500 mm yr<sup>-1</sup> and decreasing urban  
 95 warming intensities for warmer climates<sup>5</sup>. Apart from the considerably higher values found for  $SUHI_{18y}$   
 96 compared to  $SUHI_{seas}$ , the large-scale patterns in  $SUHI_{18y}$  are in general consistent with those observed  
 97 for  $SUHI_{seas}$  (see **Fig. S2a**) and found in earlier studies for city-scale seasonal means<sup>3,5</sup>. We notice that  
 98 areas characterized by strong climatic variability during the warm season, e.g. monsoon regions, usually  
 99 experience a stronger difference between seasonal averages and maxima (**Fig. S2b,c**) that can be linked to  
 100 more distinctive seasonal hysteretic cycles of urban and rural temperatures<sup>34</sup>.

101

## 102 Long-term trends in SUHI maxima

103 We find that across all urban centres worldwide SUHI maxima ( $SUHI_{1y}$ ) have increased on average by  
 104 nearly 1.04 K, or 0.06K yr<sup>-1</sup>, between 2003 and 2020 (**Fig. 2**). Eastern Asia shows the strongest rise of 0.12 K  
 105 yr<sup>-1</sup>, which can be linked to the rapid urbanisation in the region<sup>10</sup>. This is exemplified by the city of Tianjin,  
 106 where the urban area nearly quadruplicated between 1980 and 2010<sup>35</sup> and the trend in  $SUHI_{1y}$  locally  
 107 exceeds 0.3 K yr<sup>-1</sup> (**Fig. 2n**). Despite the general trend of urbanisation and consequent urban warming in the  
 108 region<sup>36</sup>, some cities in Eastern Asia show distinctive signs of declining population in inner-city areas<sup>37</sup>. This  
 109 can cause a downward trend in SUHI in shrinking city parts, such as in Seoul, where after 2000 the  
 110 population decline and requalification of the central business district led to reduced SUHI intensities in the

111 city centre<sup>38</sup> (**Fig. 2m**). While the process of city shrinking is emerging in Asian cities, it has been observed  
112 since many decades in US and Europe<sup>39</sup>, and even in developing countries a number of large cities have  
113 been affected by this phenomenon<sup>40</sup>. In many cases this is accompanied by suburbanisation, which shifts  
114 the burden to newly built-up suburbs where extreme SUHI can rise rapidly.

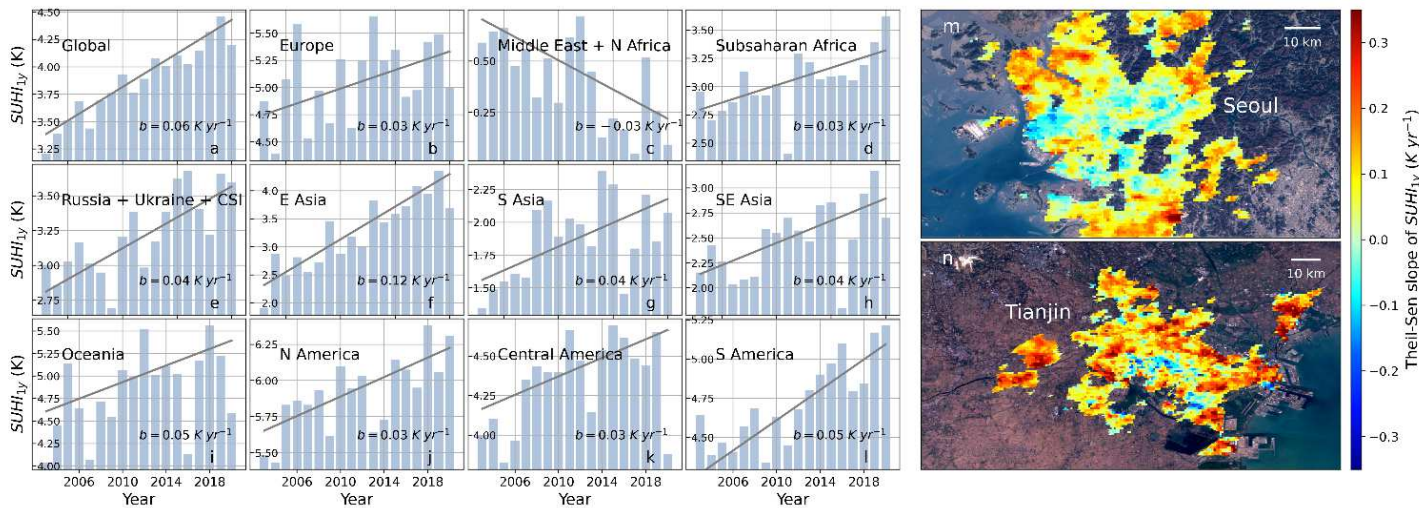
115 Despite the strong urbanisation in Southern and South Eastern Asia, but also in sub-Saharan Africa<sup>10</sup>, the  
116 rate of increase in extreme daytime UHI intensity is two to four times lower compared to Eastern Asia. This  
117 conforms to the effects of background climate on urban surface warming, which is more pronounced in  
118 temperate regions compared to more arid and tropical regions. In the very hot and dry climate of the  
119 Middle East and North Africa the trend is negative as urbanisation generally results in heat sinks.

120 Extreme urban surface warming has increased less strongly also in North America (0.03 K yr<sup>-1</sup>), Europe (0.03  
121 K yr<sup>-1</sup>), South-America (0.05 K yr<sup>-1</sup>), and Oceania (0.05 K yr<sup>-1</sup>). With already more than 70% of population  
122 living in urban centres in these regions<sup>41</sup>, urbanisation in recent decades has been lower compared to  
123 strongly developing areas. However, at present these regions still show the highest extreme SUHI  
124 intensities, with average  $SUHI_{1y}$  above 6 K for cities in North-America, close to 5.5 K in Oceania and  
125 Europe, and around 5 K in South-America.

126 Extreme SUHI intensities show in general a stronger increasing trend in time compared to median warm-  
127 season values (**Fig. S3**), but there are strong geographic differences. In South-America,  $SUHI_{1y}$  has  
128 increased by 0.05 K yr<sup>-1</sup> compared to 0.02 K yr<sup>-1</sup> for  $SUHI_{seas}$ , implying extreme urban surface warming has  
129 increased more than double the rate of the seasonal values. Also in Europe and Russia extreme SUHI  
130 intensities have clearly risen more. In sub-Saharan Africa there is no trend in  $SUHI_{seas}$  while  $SUHI_{1y}$  has  
131 increased by nearly 0.5 K between 2003 and 2020. In South Asia,  $SUHI_{seas}$  has become slightly less  
132 negative, while  $SUHI_{1y}$  increased from 1.4 K to nearly 2 K on average over the region (**Fig. 2**).

133 A generally upward trend in temporally-aggregated urban warming has been reported before, with strong  
134 variations between cities<sup>23,24</sup>. This is driven by the continued urbanisation around the world<sup>7,10</sup>, the  
135 greening of natural vegetation<sup>9</sup> and cropland<sup>42</sup> in rural areas, and modulated by background climate<sup>5,16</sup> and  
136 artificial dynamics<sup>38,43</sup>. The more pronounced trend in  $SUHI_{1y}$  compared to  $SUHI_{seas}$  suggests a higher  
137 sensitivity of extreme SUHI to urbanisation. Current understanding does not indicate that global warming  
138 directly enhances differences in rural-urban warming<sup>22</sup>, but the observed increase in heatwave days almost  
139 everywhere since the 1950s<sup>8</sup> and possible synergies between heat waves and SUHI<sup>33</sup> can partially explain  
140 the stronger increase in SUHI extremes. The amplification of greenness-climate feedbacks during extreme  
141 climate conditions<sup>44</sup> further suggests stronger positive effects of greening of non-urban areas on extreme  
142 SUHI compared to temporally-aggregated urban warming.

143



144

145 **Fig. 2 | Trend in yearly SUHI maxima of the warm season.** Trend of  $SUHI_{1y}$  for the globe (a) and in different macro-areas (b-l). In  
 146 each panel the Theil-Sen slope<sup>7</sup> is reported (coefficient b). For the globe and all macro-areas the slope is significant beyond the 95%  
 147 confidence. m-n, Maps of the trend (in  $K yr^{-1}$ ) in Seoul (m) and Tianjin (n). Figure S4 shows the pixels built-up between 2000 and  
 148 2015 according to GHSL.

149

## 150 A zoom on city scale variability

151 A zoom on 14 megacities spread over the different continents reveals highly diversified intra-city pictures of  
 152 extreme surface urban warming (**Fig. 3**). Across these urban centres,  $SUHI_{18y}$  varies on average by 12.8 K  
 153 (**Fig. 3, Table S2**), with the highest spatial variability observed in Tokyo ( $0.9 \leq SUHI_{18y} \leq 17.6$  K) and New  
 154 York ( $0.1 \leq SUHI_{18y} \leq 16$  K), and the lowest in Paris ( $2.1 \leq SUHI_{18y} \leq 12.7$  K) and London ( $0.8 \leq SUHI_{18y} \leq 10$  K).

155 While each city has its own unique combination of climate, geography, and internal structure, some  
 156 common patterns can be observed. Hotspots are often found in industrial parts of cities, where waste heat,  
 157 the use of dark construction material and absence of vegetation can result in high SUHI intensities<sup>45</sup>. For  
 158 example, in New York particularly high values of  $SUHI_{18y}$  can be observed South of Newark, where the  
 159 international airport, a railroad and other industrial facilities are located (**Fig. S5**). In Paris the hotspots of  
 160  $SUHI_{18y}$  are east of Saint-Denis and near Chevilly Larue, both areas with large industrial complexes  
 161 (Figure S6). Similar examples can be found for all of the examined cities (**Fig. 2**).

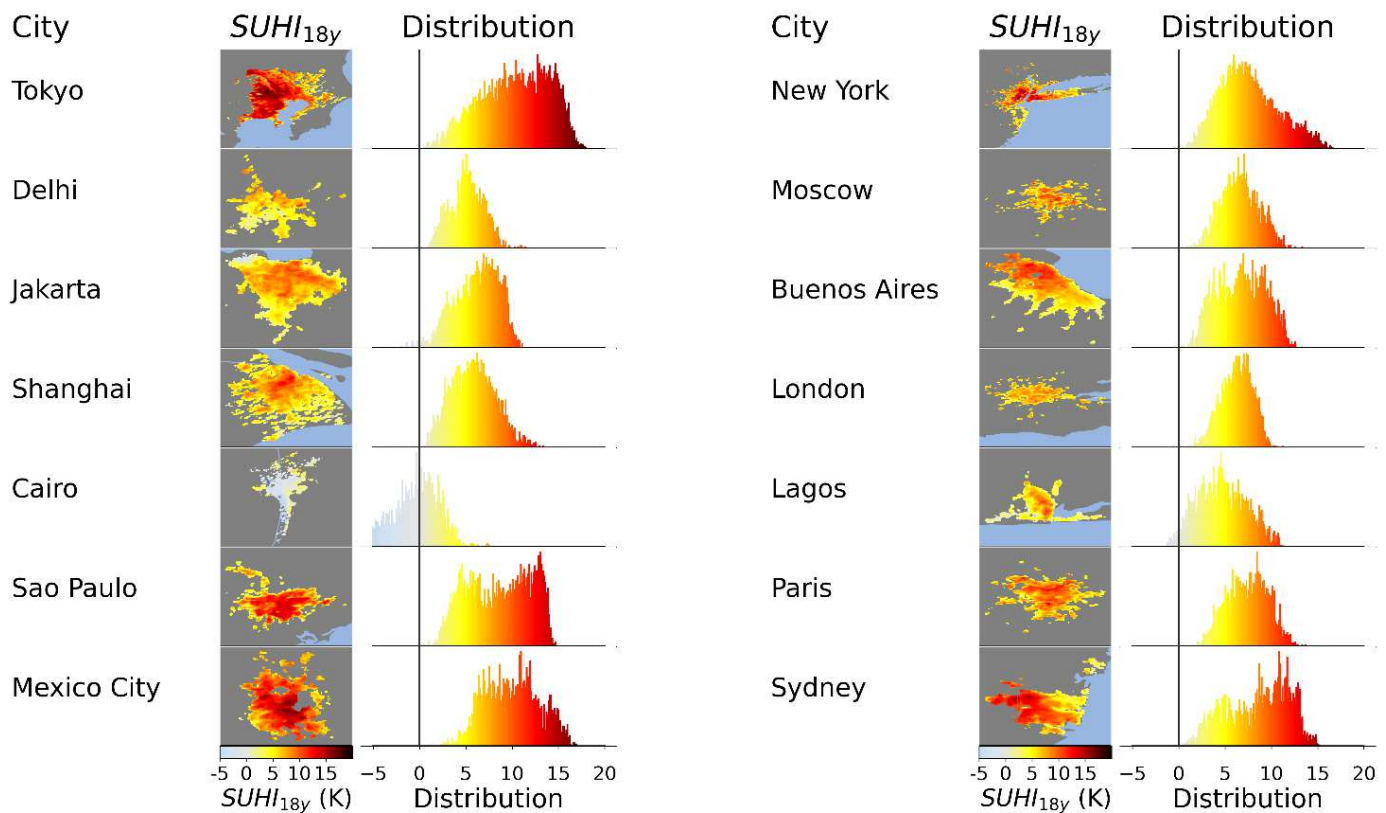
162 In Mexico City high values of  $SUHI_{18y}$  can be found in areas characterised by a high concentration of slums,  
 163 such as Ciudad Nezahualcoyotl and Iztapalapa (Figures S7). This corroborates the link between the chaotic,  
 164 dense and unregulated urbanisation typical of slums and intense heat exposure<sup>46</sup>. Combined with poverty,  
 165 poor housing conditions and little access to cooling options this poses serious health threats to people<sup>47</sup>.

166 Urban parks and green zones often correspond to relatively cooler areas. This can be observed, for  
 167 example, for the forest areas in Hachioji<sup>48</sup>, at the Sayama lake, and in the Chiyoda park in Tokyo, the Bois de  
 168 Boulogne and the Bois de Vincennes in Paris, Hampstead Heath in London, La Tourette Park in New York  
 169 (**Fig. S8, S6, S9, S5**). Water bodies within the city can also dampen  $SUHI_{18y}$  intensity, as exemplified by the  
 170 River Thames in London (**Fig. S9**). These findings confirm the important role of urban green and water in  
 171 the mitigation of SUHI<sup>17</sup>. In coastal cities, proximity to the sea can mitigate  $SUHI_{18y}$ , as can be observed in  
 172 Buenos Aires, Sydney and Jakarta, but sea breeze cooling effects can be inhibited by tall buildings on the  
 173 seafront or inner city<sup>22</sup>.

174 The low values of  $SUHI_{18y}$  observed in Cairo are explained by the drier climate, with surrounding deserts  
 175 that warm up fast in clear sky conditions, and scarce vegetation and evapotranspiration cooling. Partially

176 located upstream of the Nile delta, the city lays in a more humid, vegetated area and even  $SUHI_{18y}$  is low  
177 or negative (down to below -5 K).

178



179

180 **Fig. 3 | Distribution of warm-season extreme SUHI in megacities.** Maps (left panels) and histograms (right panels) of warm-season  
181 3-day SUHI maximum over the 18 years analysed ( $SUHI_{18y}$ ). Considered are all urban pixels within the Functional Urban Areas for  
182 each of the 14 world megacities.

183

## 184 Conclusions

185 Our results reveal relevant spatiotemporal variability in SUHI that is not captured by previous global  
186 coarser-grained spatiotemporal representations of SUHI<sup>3,5</sup>. Short-term (3-day) SUHI maxima can be several  
187 degrees higher than seasonally estimated SUHI, with differences up to 10 K and more, while they can vary  
188 by an order of magnitude within cities. While SUHI extremes are already intensifying, continued  
189 urbanisation<sup>10</sup>, a growing number of slum dwellers, and a further rise in the frequency and intensity of hot  
190 spells with global warming<sup>49</sup>, could elevate urban heat stress and consequent health risk to unprecedented  
191 levels in the most exposed and vulnerable city neighbourhoods in the near future. The management of  
192 extreme heat in cities will therefore be a major challenge to improve health and the urban environment.  
193 Global urban science can support this process by building fine-grained UHI models applicable across urban  
194 settlements worldwide, including under-studied regions and smaller cities<sup>50</sup>, in order to forge new  
195 knowledge on urban warming extremes and their drivers. The dataset produced in this study, available on  
196 the Google Earth Engine, offers this opportunity.

197

198

199

200

201

202

## 203 Bibliography

- 204 1. Oke, T. R. The energetic basis of the urban heat island. *Q. J. R. Meteorol. Soc.* (1982).  
205 doi:10.1002/qj.49710845502
- 206 2. Sera, F. *et al.* How urban characteristics affect vulnerability to heat and cold: A multi-country  
207 analysis. *Int. J. Epidemiol.* (2019). doi:10.1093/ije/dyz008
- 208 3. Peng, S. *et al.* Surface urban heat island across 419 global big cities. *Environ. Sci. Technol.* (2012).  
209 doi:10.1021/es2030438
- 210 4. Clinton, N. & Gong, P. MODIS detected surface urban heat islands and sinks: Global locations and  
211 controls. *Remote Sens. Environ.* (2013). doi:10.1016/j.rse.2013.03.008
- 212 5. Manoli, G. *et al.* Magnitude of urban heat islands largely explained by climate and population.  
213 *Nature* (2019). doi:10.1038/s41586-019-1512-9
- 214 6. Chakraborty, T. & Lee, X. A simplified urban-extent algorithm to characterize surface urban heat  
215 islands on a global scale and examine vegetation control on their spatiotemporal variability. *Int. J.*  
216 *Appl. Earth Obs. Geoinf.* **74**, 269–280 (2019).
- 217 7. Gong, P. *et al.* Annual maps of global artificial impervious area (GAIA) between 1985 and 2018.  
218 *Remote Sens. Environ.* **236**, 111510 (2020).
- 219 8. Perkins-Kirkpatrick, S. E. & Lewis, S. C. Increasing trends in regional heatwaves. *Nat. Commun.*  
220 (2020). doi:10.1038/s41467-020-16970-7
- 221 9. Yao, R., Wang, L., Huang, X., Gong, W. & Xia, X. Greening in Rural Areas Increases the Surface Urban  
222 Heat Island Intensity. *Geophys. Res. Lett.* **46**, 2204–2212 (2019).
- 223 10. United Nations, Department of Economic and Social Affairs, P. D. The World 's Cities in 2018.  
224 *World's Cities 2018 - Data Bookl. (ST/ESA/SER.A/417)* (2018).
- 225 11. Dosio, A., Mentaschi, L., Fischer, E. M. & Wyser, K. Extreme heat waves under 1.5 °c and 2 °c global  
226 warming. *Environ. Res. Lett.* **13**, (2018).
- 227 12. Zhao, Q., Zhu, Z., Zeng, H., Zhao, W. & Myneni, R. B. Future greening of the Earth may not be as  
228 large as previously predicted. *Agric. For. Meteorol.* **292–293**, 108111 (2020).
- 229 13. Sherwood, S. C. & Huber, M. An adaptability limit to climate change due to heat stress. *Proc. Natl.*  
230 *Acad. Sci. U. S. A.* (2010). doi:10.1073/pnas.0913352107
- 231 14. Arnfield, A. J. Two decades of urban climate research: a review of turbulence, exchanges of energy  
232 and water, and the urban heat island. *Int. J. Climatol.* **23**, 1–26 (2003).
- 233 15. Zhou, D. *et al.* Satellite remote sensing of surface urban heat islands: Progress, challenges, and  
234 perspectives. *Remote Sensing* (2019). doi:10.3390/rs11010048
- 235 16. Zhao, L., Lee, X., Smith, R. B. & Oleson, K. Strong contributions of local background climate to urban  
236 heat islands. *Nature* (2014). doi:10.1038/nature13462
- 237 17. Weng, Q., Lu, D. & Schubring, J. Estimation of land surface temperature-vegetation abundance  
238 relationship for urban heat island studies. *Remote Sens. Environ.* (2004).

- 239 doi:10.1016/j.rse.2003.11.005
- 240 18. Li, X., Zhou, Y., Asrar, G. R., Imhoff, M. & Li, X. The surface urban heat island response to urban  
241 expansion: A panel analysis for the conterminous United States. *Sci. Total Environ.* (2017).  
242 doi:10.1016/j.scitotenv.2017.06.229
- 243 19. Zhou, B., Rybski, D. & Kropp, J. P. The role of city size and urban form in the surface urban heat  
244 island. *Sci. Rep.* (2017). doi:10.1038/s41598-017-04242-2
- 245 20. Chakraborty, T. & Lee, X. A simplified urban-extent algorithm to characterize surface urban heat  
246 islands on a global scale and examine vegetation control on their spatiotemporal variability. *Int. J.*  
247 *Appl. Earth Obs. Geoinf.* (2019). doi:10.1016/j.jag.2018.09.015
- 248 21. Zhou, D., Zhao, S., Liu, S., Zhang, L. & Zhu, C. Surface urban heat island in China's 32 major cities:  
249 Spatial patterns and drivers. *Remote Sens. Environ.* (2014). doi:10.1016/j.rse.2014.05.017
- 250 22. Masson, V., Lemonsu, A., Hidalgo, J. & Voogt, J. Urban Climates and Climate Change. *Annu. Rev.*  
251 *Environ. Resour.* **45**, 411–444 (2020).
- 252 23. Ajaaj, A. A., Mishra, A. K. & Khan, A. A. Urban and peri-urban precipitation and air temperature  
253 trends in mega cities of the world using multiple trend analysis methods. *Theor. Appl. Climatol.*  
254 (2018). doi:10.1007/s00704-017-2096-7
- 255 24. Varquez, A. C. G. & Kanda, M. Global urban climatology: a meta-analysis of air temperature trends  
256 (1960–2009). *npj Clim. Atmos. Sci.* (2018). doi:10.1038/s41612-018-0042-8
- 257 25. Wang, J., Zhou, W. & Wang, J. Time-Series Analysis Reveals Intensified Urban Heat Island Effects but  
258 without Significant Urban Warming. *Remote Sens.* **11**, 2229 (2019).
- 259 26. Armson, D., Stringer, P. & Ennos, A. R. The effect of tree shade and grass on surface and globe  
260 temperatures in an urban area. *Urban For. Urban Green.* **11**, 245–255 (2012).
- 261 27. Tzavali, A., Paravantis, J. P., Mihalakakou, G., Fotiadi, A. & Stigka, E. Urban heat island intensity: A  
262 literature review. *Fresenius Environ. Bull.* (2015).
- 263 28. Meehl, G. A. & Tebaldi, C. More intense, more frequent, and longer lasting heat waves in the 21st  
264 century. *Science* (2004). doi:10.1126/science.1098704
- 265 29. Nitschke, M., Tucker, G. R. & Bi, P. Morbidity and mortality during heatwaves in metropolitan  
266 Adelaide. *Med. J. Aust.* (2007). doi:10.5694/j.1326-5377.2007.tb01466.x
- 267 30. Gao, J. *et al.* Impact of extreme high temperature on mortality and regional level definition of heat  
268 wave: A multi-city study in China. *Sci. Total Environ.* (2015). doi:10.1016/j.scitotenv.2014.10.028
- 269 31. Corbane, C. *et al.* Convolutional neural networks for global human settlements mapping from  
270 Sentinel-2 satellite imagery. *Neural Comput. Appl.* (2020). doi:10.1007/s00521-020-05449-7
- 271 32. Scott, A. A., Waugh, D. W. & Zaitchik, B. F. Reduced Urban Heat Island intensity under warmer  
272 conditions. *Environ. Res. Lett.* (2018). doi:10.1088/1748-9326/aabd6c
- 273 33. Zhao, L. *et al.* Interactions between urban heat islands and heat waves. *Environ. Res. Lett.* (2018).  
274 doi:10.1088/1748-9326/aa9f73
- 275 34. Manoli, G., Fatichi, S., Bou-Zeid, E. & Katul, G. G. Seasonal hysteresis of surface urban heat islands.  
276 *Proc. Natl. Acad. Sci.* **117**, 7082–7089 (2020).
- 277 35. Wu, W., Zhao, S., Zhu, C. & Jiang, J. A comparative study of urban expansion in Beijing, Tianjin and  
278 Shijiazhuang over the past three decades. *Landsc. Urban Plan.* **134**, 93–106 (2015).
- 279 36. Yang, Q., Huang, X. & Tang, Q. The footprint of urban heat island effect in 302 Chinese cities:

- 280 Temporal trends and associated factors. *Sci. Total Environ.* (2019).  
281 doi:10.1016/j.scitotenv.2018.11.171
- 282 37. Liu, Z., Liu, S. & Song, Y. Understanding urban shrinkage in China: Developing a multi-dimensional  
283 conceptual model and conducting empirical examination from 2000 to 2010. *Habitat Int.* (2020).  
284 doi:10.1016/j.habitatint.2020.102256
- 285 38. Hong, J.-W., Hong, J., Kwon, E. E. & Yoon, D. K. Temporal dynamics of urban heat island correlated  
286 with the socio-economic development over the past half-century in Seoul, Korea. *Environ. Pollut.*  
287 **254**, 112934 (2019).
- 288 39. Martinez-Fernandez, C. *et al.* Shrinking cities in Australia, Japan, Europe and the USA: From a global  
289 process to local policy responses. *Prog. Plann.* (2016). doi:10.1016/j.progress.2014.10.001
- 290 40. *State of the world's cities 2008/2009: Harmonious cities. State of the World's Cities 2008/2009:*  
291 *Harmonious Cities* (2012). doi:10.4324/9781849772624
- 292 41. Carneiro Freire, S. M. *et al.* *Atlas of the Human Planet 2019.* (2019). doi:10.2760/014159
- 293 42. Chen, C. *et al.* China and India lead in greening of the world through land-use management. *Nat.*  
294 *Sustain.* **2**, 122–129 (2019).
- 295 43. Nichol, J. E., Choi, S. Y., Wong, M. S. & Abbas, S. Temperature change and urbanisation in a multi-  
296 nucleated megacity: China's Pearl River Delta. *Urban Clim.* **31**, 100592 (2020).
- 297 44. Forzieri, G., Alkama, R., Miralles, D. G. & Cescatti, A. Satellites reveal contrasting responses of  
298 regional climate to the widespread greening of Earth. *Science* **356**, 1180–1184 (2017).
- 299 45. Portela, C. I., Massi, K. G., Rodrigues, T. & Alcântara, E. Impact of urban and industrial features on  
300 land surface temperature: Evidences from satellite thermal indices. *Sustain. Cities Soc.* (2020).  
301 doi:10.1016/j.scs.2020.102100
- 302 46. Wang, J., Kuffer, M., Sliuzas, R. & Kohli, D. The exposure of slums to high temperature: Morphology-  
303 based local scale thermal patterns. *Sci. Total Environ.* **650**, 1805–1817 (2019).
- 304 47. Teare, J. *et al.* Dwelling Characteristics Influence Indoor Temperature and May Pose Health Threats  
305 in LMICs. *Ann. Glob. Heal.* **86**, (2020).
- 306 48. Tran, H., Uchihama, D., Ochi, S. & Yasuoka, Y. Assessment with satellite data of the urban heat island  
307 effects in Asian mega cities. *Int. J. Appl. Earth Obs. Geoinf.* (2006). doi:10.1016/j.jag.2005.05.003
- 308 49. Russo, S. *et al.* Half a degree and rapid socioeconomic development matter for heatwave risk. *Nat.*  
309 *Commun.* (2019). doi:10.1038/s41467-018-08070-4
- 310 50. Acuto, M. Give cities a seat at the top table. *Nature* (2016). doi:10.1038/537611a
- 311 51. Wan, Z. & Li, Z. L. MODIS land surface temperature and emissivity. in *Remote Sensing and Digital*  
312 *Image Processing* **11**, 563–577 (2011).
- 313 52. Corbane, C. *et al.* Convolutional Neural Networks for Global Human Settlements Mapping from  
314 Sentinel-2 Satellite Imagery. *arXiv e-prints* (2020).
- 315 53. Gorelick, N. *et al.* Google Earth Engine: Planetary-scale geospatial analysis for everyone. *Remote*  
316 *Sens. Environ.* **202**, 18–27 (2017).
- 317 54. Hart, L. G., Larson, E. H. & Lishner, D. M. Rural Definitions for Health Policy and Research. *Am. J.*  
318 *Public Health* **95**, 1149–1155 (2005).
- 319 55. Pekel, J.-F., Cottam, A., Gorelick, N. & Belward, A. S. High-resolution mapping of global surface water  
320 and its long-term changes. *Nature* 1–19 (2016). doi:10.1038/nature20584

- 321 56. Stewart, I. D. A systematic review and scientific critique of methodology in modern urban heat  
322 island literature. *International Journal of Climatology* (2011). doi:10.1002/joc.2141
- 323 57. USGS. SRTM Topography. *SRTM Doc. 2.1*, [http://dds.cr.usgs.gov/srtm/version\\_1/Documentatio](http://dds.cr.usgs.gov/srtm/version_1/Documentatio)  
324 (2009).
- 325 58. Hartmann, D. L. *Global physical climatology: Second Edition. Global Physical Climatology: Second*  
326 *Edition* (2015). doi:10.1016/C2009-0-00030-0
- 327 59. Schiavina, M., Moreno-monroy, A., Maffenini, L. & Veneri, P. GHSL-OECD Functional Urban Areas.  
328 (2019). doi:10.2760/67415
- 329 60. Dijkstra, L., Poelman, H. & Veneri, P. The EU-OECD definition of a functional urban area. *OECD Reg.*  
330 *Dev. Work. Pap. Éditions OCDE* (2019). doi:doi.org/10.1787/d58cb34d-en
- 331 61. Moreno-Monroy, A. I., Schiavina, M. & Veneri, P. Metropolitan areas in the world. Delineation and  
332 population trends. *J. Urban Econ.* 103242 (2020). doi:10.1016/j.jue.2020.103242
- 333 62. Song, Y., Achberger, C. & Linderholm, H. W. Rain-season trends in precipitation and their effect in  
334 different climate regions of China during 1961-2008. *Environ. Res. Lett.* (2011). doi:10.1088/1748-  
335 9326/6/3/034025
- 336 63. Dash, S. K., Kulkarni, M. A., Mohanty, U. C. & Prasad, K. Changes in the characteristics of rain events  
337 in India. *J. Geophys. Res. Atmos.* (2009). doi:10.1029/2008JD010572
- 338 64. Nicholson, S. E., Some, B. & Kone, B. An analysis of recent rainfall conditions in West Africa,  
339 including the rainy seasons of the 1997 El Nino and the 1998 La Nina years. *J. Clim.* (2000).  
340 doi:10.1175/1520-0442(2000)013<2628:AAORRC>2.0.CO;2
- 341 65. Theil, H. A Rank-Invariant Method of Linear and Polynomial Regression Analysis. in (1992).  
342 doi:10.1007/978-94-011-2546-8\_20

343

## 344 Methods

345

346 Mapping land surface temperature and built-up surfaces

347 Daily data of Land Surface Temperature (*LST*) were taken from the MODIS Aqua product of global Land  
348 Surface Temperature/Emissivity (MYD11A1 version 6<sup>1</sup>) for the period from January 2003 until December  
349 2020. This 1-km resolution dataset was chosen for its quasi-daily coverage of the world surface. Our focus  
350 in on daytime SUHI and satellite Aqua was preferred to Terra because it provides measurements in the  
351 early afternoon, approximately at the time of highest solar radiation and maximum daily surface  
352 temperature.

353 The extent of built-up surfaces used to define urban and non-urban areas has also been mapped by means  
354 of satellite imagery classification. We used the most recent version of the Global Human Settlement Layer  
355 (GHSL<sup>2</sup>), based on Sentinel-2. It is based on convolution neural network modelling for pixel-wise image  
356 classification of built-up areas and provides at 10-m resolution the probability (between 0 and 100%) of a  
357 pixel to belong to the class built-up for the year 2018.

358 The handling of the large datasets and the analysis of SUHI as described below was carried out on the  
359 Google Earth Engine<sup>3</sup>.

360

## 361 Estimation of SUHI

362 SUHI is defined as the difference in LST between urban and non-urban or rural areas. The term rural, which  
363 acquires distinct semantics in different literary contexts, is broadly used in scientific literature to indicate  
364 any type of non-urban territory<sup>4</sup>. Here it identifies any pixel that is not built-up. The resolution of the built-  
365 up information from GHSL (10 m) is higher than that of the LST from MODIS (1 km). For each MODIS 1-km  
366 pixel the mean built-up probability was estimated for the year 2018 by averaging the probability values of  
367 the 10-m GHSL pixels contained inside of it. Then, MODIS pixels with a mean probability >15% were  
368 considered as built-up. The minimum threshold suggested to be considered as built-up is a probability of  
369 20%<sup>5</sup>. However, in our case the main objective is the exclusion of built-up pixels from the computation of  
370 the surrounding non-urban temperature, which justifies the choice of a lower cut-off. The detection of the  
371 built-up pixels was carried out solely for 2018, the reference year of the latest GHSL dataset.

372 Although water bodies can dampen SUHI in nearby and downwind locations, they should be excluded from  
373 the surrounding rural area considered in the calculation of SUHI, as that would artificially inflate SUHI  
374 values. For the detection of water bodies, we used the Global Surface Water (GSW) dataset<sup>6</sup> available at  
375 30-m resolution. For each MODIS pixel, the percentage of surface occupied by water was estimated from  
376 GSW, and 1-km pixels with water presence >15% were excluded from the computation. The latest available  
377 raster of water presence was employed (year 2019).

378 The intensity of the SUHI was estimated from LST by means of a kernel-based approach whereby the same  
379 procedure was applied to all the urban pixels of all the imagery available in MYD11A1. For each 1-km built-  
380 up pixel the LST was obtained directly from MODIS and is denoted by  $LST_{urban}$ . The corresponding value for  
381 the rural surroundings ( $LST_{rural}$ ), was computed as the median LST of all non-built-up non-water pixels  
382 within a kernel consisting of a 70 km-side square centred on the built-up pixel. This size guarantees that in  
383 the majority of the cities, for any built-up pixel there are at least 500 non-built-up pixels for the  
384 computation of  $LST_{rural}$ . The only city where this condition is violated in a part of the urban area is Shanghai,  
385 for which a double-size kernel (a 140 km-side square) was used. The SUHI was then computed as the  
386 difference between the  $LST$  of the built-up pixel ( $LST_{urban}$ ) and the surrounding non-urban area ( $LST_{rural}$ ):

$$SUHI = LST_{urban} - LST_{rural} \quad 1.$$

387

388 Elevation is an important factor that influences LST and placing urban and rural pixels at similar elevation is  
389 required to isolate the effect of urbanisation on SUHI<sup>7</sup>. Consequently, the temperature data of pixels at  
390 different altitude should be corrected before being able to compare them. To account for the effects of  
391 surface relief we used the Shuttle Radar Topography Mission data provided by the U.S. Geological Survey  
392 (USGS SRTM<sup>8</sup>) at 100-m resolution. The LST of each pixel was corrected to the mean altitude of the 70 km-  
393 size square centred in the pixel (140 km in proximity of Shanghai). The adjustment was done considering an  
394 environmental lapse rate of -6.5 K per 1000 m of altitude<sup>9</sup>.

395 The kernel-based approach comes with advantages with respect to techniques relying on a definition of  
396 urban area based on population or other socioeconomic indicators, in terms of robustness and  
397 reproducibility. It has only 2 degrees of freedom: the cut-off to define the built-up pixels (15% of built-up  
398 probability), and the kernel size (70 km, everywhere with the exception of Shanghai where the kernel size is  
399 140 km). Furthermore, its application to all the built-up pixels, including the ones not located in urban areas  
400 delineated based on socioeconomic indicators, enables the possible future study of the urban-non urban  
401 continuum.

402

## 403 SUHI in Functional Urban Areas

404 Though the estimation of SUHI was carried out and stored for all built-up 1-km pixels worldwide, we report  
405 spatial and temporal statistics over built-up pixels enclosed within the spatial boundaries of 9028  
406 Functional Urban Areas (FUA)<sup>10</sup>. FUA are cities and their surroundings, composed of high-density urban  
407 centres with at least 50 thousand people plus their surrounding commuting zones<sup>11</sup>. They are used here to  
408 identify urban contexts, leaving out small and isolated extra-urban centres made up of few built-up pixels.  
409 Today 53% of the world population (3.9 billion people) live inside FUA<sup>12</sup>. Overall, more than 1,200,000 1-km  
410 urban pixels (i.e. built-up pixels located in a FUA) were considered in the discussion.

411

## 412 SUHI during periods of heat stress

413 The analysis presented in this manuscript focuses on SUHI during the warm season, when human heat  
414 stress is typically highest<sup>13–15</sup>. Past studies used a temperate-zone definition of summer, i.e., the months of  
415 June, July, August (JJA) for the Northern Hemisphere (NH), the months of December, January, February  
416 (DJF) for the Southern Hemisphere (SH)<sup>13,16–18</sup>. However, in some tropical and subtropical areas, these  
417 months may partially coincide with the raining season<sup>19–21</sup>. This reduces the likelihood of intense heatwaves  
418 and the number of reliable observations of SUHI. Therefore, we defined the warm season as:

- 419 • For temperate and polar regions (latitude above 35°N/S), the months of JJA/DJF in the NH/SH.
- 420 • For tropical and subtropical regions (10°N/S < latitude < 35°N/S), the months of April, May, June,  
421 July, August, September (AMJJAS) in the NH, the months of October, November, December,  
422 January, February, March (ONDJFM) in the SH.
- 423 • For areas closer than 10° to the equator, characterized by persistent warm conditions, the whole  
424 year was considered.

425 Human impacts of heat are highest when conditions of high temperature last for several days<sup>22–24</sup>. In each  
426 urban pixel the daily estimates of SUHI during the warm season were therefore temporally aggregated by  
427 means of a 3-day moving average. From the resulting time-averaged time series, we estimated the  
428 following statistics for each urban pixel: (1) the warm-season medians ( $SUHI_{seas}$ ), which represents a  
429 central estimate of the SUHI in the warm season for each year between 2003–2020; (2) the 1-year maxima  
430 ( $SUHI_{1y}$ ), which represents the maximum 3-day SUHI in the warm season for each year between 2003–  
431 2020; and (3) the 18-year maximum ( $SUHI_{18y}$ ), which represents the maximum 3-day SUHI estimated over  
432 all the warm seasons between 2003–2020. The space-time statistics (medians, 95<sup>th</sup> percentiles, maxima, %  
433 above zero) of  $SUHI_{seas}$ ,  $SUHI_{1y}$ , shown in Table S1 and presented in the manuscript, were estimated by  
434 computing a pixelwise median between the annual values, and then considering the resulting spatial  
435 distribution. For  $SUHI_{18y}$ , which is not defined along a time axis, the statistics were estimated directly from  
436 the spatial raster.

437 Trends were estimated on the annual values of  $SUHI_{1y}$  and  $SUHI_{seas}$  for the world and 11 macro-regions  
438 (Europe, Middle East + North Africa, Sub-Saharan Africa, Russia + Ukraine + Commonwealth of Independent  
439 States (CIS), East Asia, South Asia, Southeast Asia, Oceania, North America, Central America, and South  
440 America).  $SUHI_{1y}$  and  $SUHI_{seas}$  estimates at pixel level were first aggregated to macro-region by taking  
441 the spatial median over urban pixels in FUA of the considered macro-region. The trend's slope was then  
442 estimated on the macro-region annual  $SUHI_{1y}$  and  $SUHI_{seas}$  values using a Theil-Sen estimator<sup>25</sup>.

443

# Figures

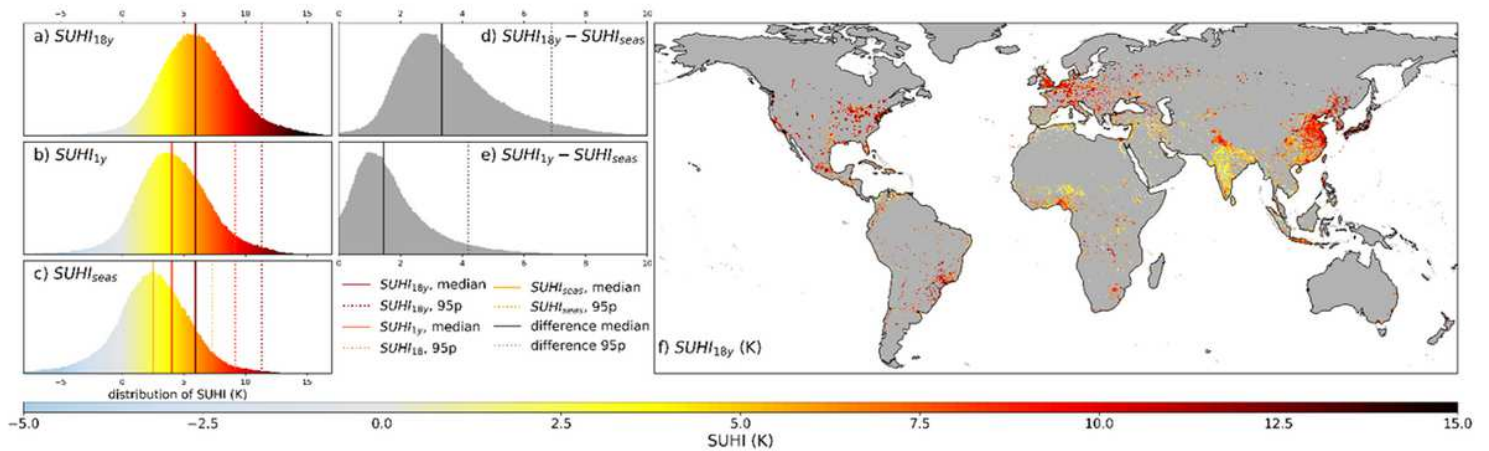


**Figure 1**

Global distribution of warm-season SUHI indices. a, Histogram across urban pixels worldwide of the pixel warm-season 3-day SUHI maximum over the 18 years analysed ( $SUHI_{18y}$ ). b, Histogram across all urban pixels worldwide of the pixel median of the yearly warm-season 3-day SUHI maxima ( $SUHI_{1y}$ ) of the 18 years analysed. c, Histogram across all urban pixels worldwide of the pixel warm-season SUHI median ( $SUHI_{seas}$ ) over the 18 years analysed. d, Histogram across all urban pixels worldwide of the pixel difference between  $SUHI_{18y}$  and the 18-year median  $SUHI_{seas}$ . e, Histogram across all urban pixels worldwide of the pixel difference between  $SUHI_{1y}$  and the 18-year median  $SUHI_{seas}$ . The solid and dashed vertical lines in the histograms in a-e represent the median and 95th percentile over all urban pixels worldwide for the respective indices and differences therein. f, Global map of warm-season 3-day SUHI maximum over the 18 years analysed ( $SUHI_{18y}$ ) in urban pixels. Urban pixels are defined as 1x1 km built-up pixels enclosed within the spatial boundaries of Functional Urban Areas (FUA). FUA are cities and their surroundings and nearly four billion people live in the 9028 FUAs worldwide. Note: The designations employed and the presentation of the material on this map do not imply the expression of any opinion whatsoever on the part of Research Square concerning the legal status of any country, territory, city or area or of its authorities, or concerning the delimitation of its frontiers or boundaries. This map has been provided by the authors.

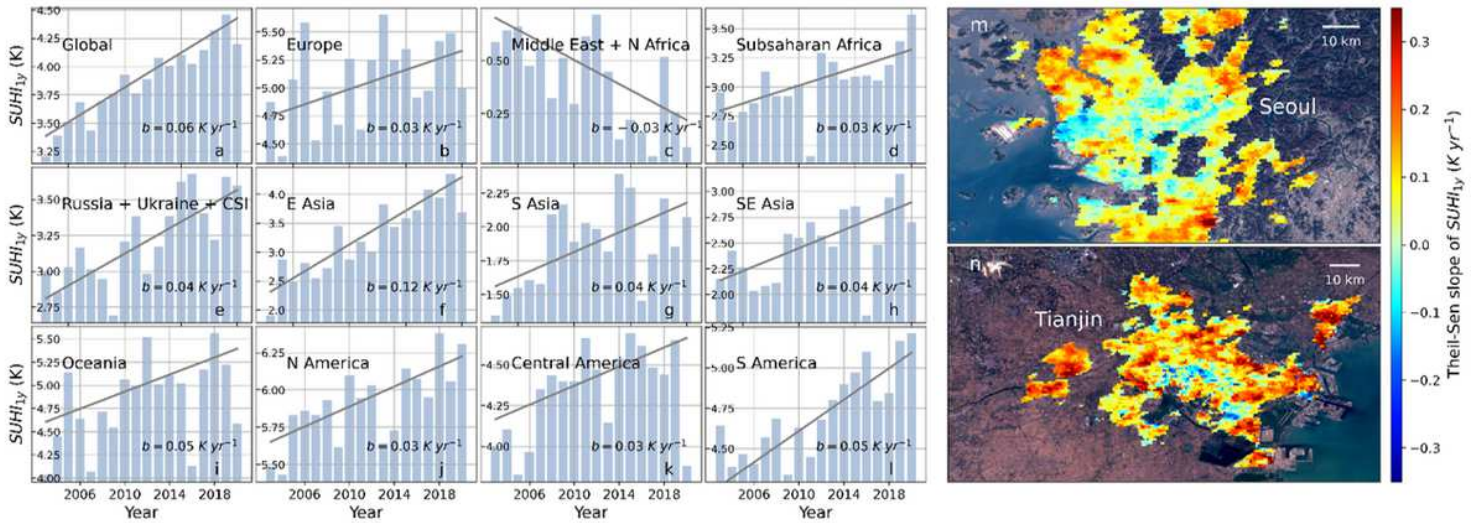


**Figure 2**

Trend in yearly SUHI maxima of the warm season. Trend of SUHI<sub>1y</sub> for the globe (a) and in different macro-areas (b-l). In each panel the Theil-Sen slope<sup>7</sup> is reported (coefficient b). For the globe and all macro-areas the slope is significant beyond the 95% confidence. m-n, Maps of the trend (in K yr<sup>-1</sup>) in Seoul (m) and Tianjin (n). Figure S4 shows the pixels built-up between 2000 and 2015 according to GHSL. Note: The designations employed and the presentation of the material on this map do not imply the expression of any opinion whatsoever on the part of Research Square concerning the legal status of any country, territory, city or area or of its authorities, or concerning the delimitation of its frontiers or boundaries. This map has been provided by the authors.

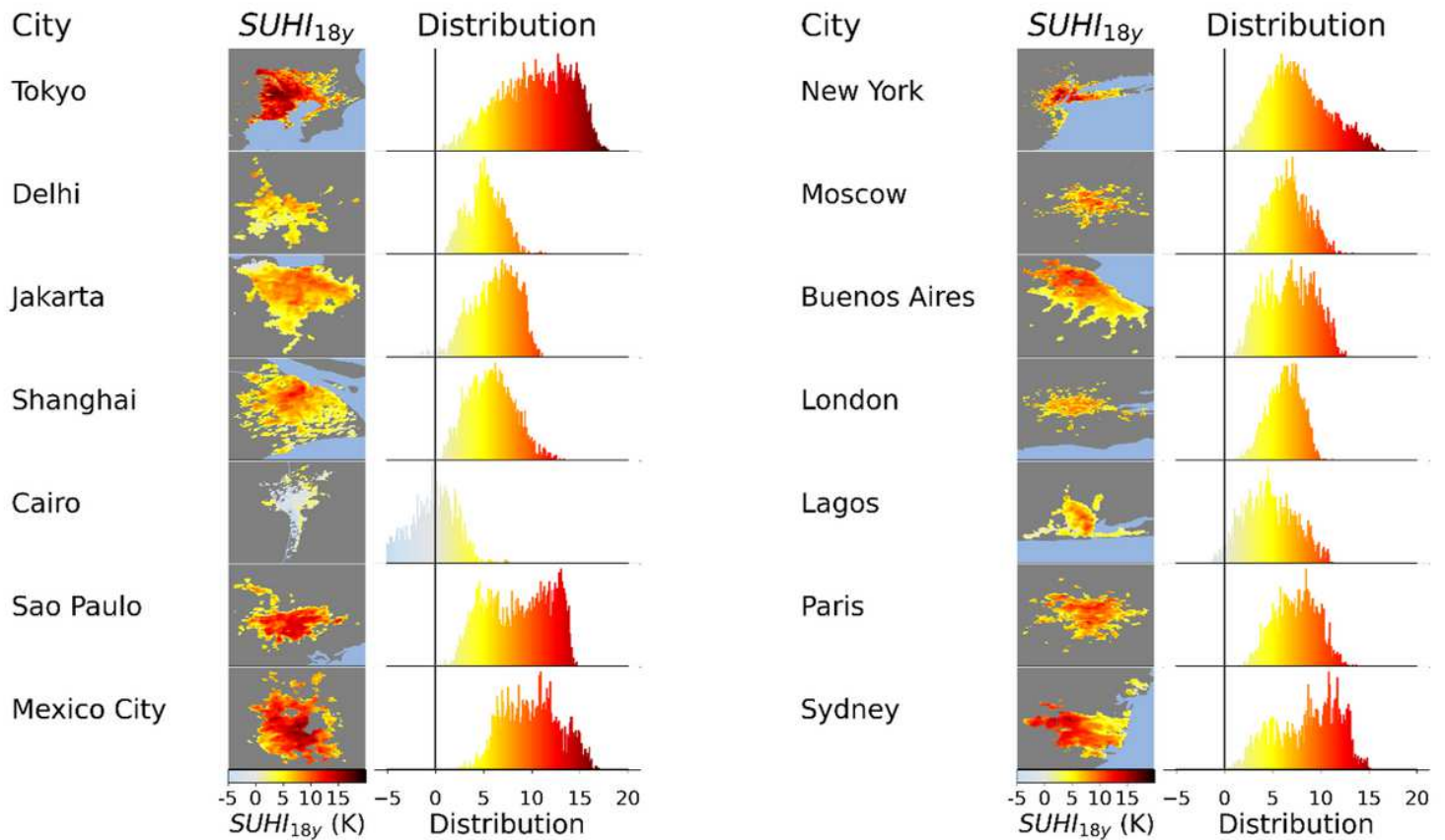


**Figure 3**

Distribution of warm-season extreme SUHI in megacities. Maps (left panels) and histograms (right panels) of warm-season 3-day SUHI maximum over the 18 years analysed (SUHI\_18y). Considered are all urban pixels within the Functional Urban Areas for each of the 14 world megacities. Note: The designations employed and the presentation of the material on this map do not imply the expression of any opinion whatsoever on the part of Research Square concerning the legal status of any country, territory, city or area or of its authorities, or concerning the delimitation of its frontiers or boundaries. This map has been provided by the authors.

## Supplementary Files

This is a list of supplementary files associated with this preprint. Click to download.

- [uhiDraftNatureSubmissionSI.docx](#)